BMES BIOMEDICAL ENGINEERING SOCIETY

ORIGINAL ARTICLE

Spatial–Temporal Oxygenation Mapping Using a Near-Infrared Optical Scanner: Towards Peripheral Vascular Imaging

Kevin Leiva[1] · Daniela Leizaola[1] · Isabella Gonzalez[1] · Valentina Dargam[2] · Haniyeh Alirezaei[1] · Kacie Kaile[1] · Edwin Robledo[1] · Joshua Hutcheson[2] · Anuradha Godavarty[1]

Abstract

Near-infrared spectroscopy (NIRS)—based peripheral perfusion, or microcirculation, can be used to assess the severity of peripheral vascular dysfunction. A low-cost, portable non-contact near-infrared optical scanner (NIROS) was developed for spatio-temporal mapping of tissue oxygenation and perfusion in tissues. In vivo validation studies were carried out on control subjects ($n = 3$) to assess the ability of NIROS to measure real-time oxygenation changes in response to an occlusion paradigm on the dorsum of the hand. NIROS captured real-time tissue oxygenation changes with 95% correlation when compared to a commercial device. A feasibility peripheral imaging study was performed in a mouse model ($n = 5$) of chronic kidney disease (CKD) induced vascular calcification to assess differences in microcirculatory peripheral tissue oxygenation. The tissue oxygenation (in terms of oxy-, deoxy-, and total hemoglobin changes) due to the occlusion paradigm was distinctly different prior to (week-6) and after the onset of vascular calcification (week-12) in the murine tails. Future work will involve extensive studies to correlate these microcirculatory tissue oxygenation changes in the peripheral tail to the vascular calcification in the heart.

Abbreviations

$\Delta[HbO]$	Effective oxyhemoglobin concentration
$\Delta[HbR]$	Effective deoxyhemoglobin concentration
$\Delta[HbT]$	Effective total hemoglobin concentration
$\Delta[StO_2]$	Effective oxygen saturation
CKD	Chronic kidney disease
GUI	Graphical user interface
HSI	Hyperspectral imaging
LDPM	Laser doppler perfusion monitoring
LSCI	Laser speckle contrast imaging
MBLL	Modified Beer-Lambert Law
NIR	Near infrared
NIRS	Near-infrared spectroscopy
NIROS	Near infrared optical scanner
PAD	Peripheral arterial disease
PCC	Pearson's correlation coefficient
ROI	Region of interest
SEM	Standard error of measurement
TcPO$_2$	Transcutaneous oxygenation measurements
VOT	Vascular occlusion test

✉ Anuradha Godavarty
godavart@fiu.edu

1 Optical Imaging Laboratory, Department of Biomedical Engineering, Florida International University, 10555 West Flagler Street, EC 2675, Miami, FL 33174, USA

2 Cardiovascular Matrix Remodeling Laboratory, Department of Biomedical Engineering, Florida International University, Miami, FL, USA

Introduction

Peripheral vascular imaging is performed to assess the microcirculation and saturation of peripheral tissue. Several non-invasive techniques have been introduced to measure tissue perfusion in the lower extremities. These techniques include hyperspectral imaging (HSI) [34], laser doppler perfusion monitoring (LDPM) [15, 25], laser speckle contrast

imaging (LSCI) [25, 34], near-infrared spectroscopy (NIRS) [2, 25], spectrophotometry [3, 25], transcutaneous oxygenation measurements (TCOM) [3] and vascular optical tomography imaging [20]. TcPO$_2$ is a gold-standard approach that is used to quantify skin oxygenation. It assesses how the vasculature responds to an oxygenation demand by inducing tissue heating (or vasodilation) to measure for partial pressure of oxygen (TcPO$_2$) under the skin. However, the technique is time-consuming (> 20 min for a single measurement) and obtains these oxygenation measurements only at discrete locations on the tissue. Additionally TCOM has $> 10\%$ intra-operator variability. [3, 25]

Perfusion-based measurements of microcirculatory blood flow are obtained using LDPM and LSCI. While these perfusion-based measurements can be obtained in real-time, they are not capable of imaging a larger peripheral region spatially. Modalities such as HSI, MSI, and NIRS measure tissue oxygenation under the skin. While HSI and MSI provide spatial maps of tissue oxygenation, NIRS techniques provide real-time measurements of tissue oxygenation at discrete point locations. NIRS has previously been used extensively in the diagnosis of peripheral arterial disease (PAD) [19, 28]. In these studies, oxygen saturation was measured in the muscles at single point location via exercise stimulating protocols in the presence of PAD. However, these low-cost NIRS devices and/or approaches are limited to muscle perfusion at point locations, making the approach subjective (as it depends on accurate NIRS probe placement) and inconsistent across patients. There is a need for imaging modalities that are capable of both spatial and temporal-based peripheral vascular imaging to map microcirculatory physiological changes under the skin across a wide-area of the peripheries and dynamically.

A low-cost non-contact near-infrared optical scanner (NIROS) that is capable of spatio-temporal-based tissue oxygenation mapping and perfusion in tissues was recently developed. Unlike LDPM that maps dynamic changes in perfusion (or blood flow at a single point location), the NIRS-based approach implemented in NIROS can obtain these near-real-time tissue oxygenation-based perfusion maps across a wide-field region of the imaged peripheries. Our approach can measure dynamically changing 2D spatial tissue oxygenation maps (in terms of hemoglobin concentration parameters) at the peripheries. Imaging across the entire peripheral region thus reduces subjectivity when clinically applied. These near real-time spatio-temporal maps of tissue oxygenation changes in the peripheries can map vascular response to underlying peripheral issues upon introducing a stimulus to induce vascular changes.

This study aims to initially validate the NIROS device for its ability to map for spatio-temporal changes in response to a stimulus that alters the peripheral tissue oxygenated flow under the skin. Following the validation study, we will assess the applicability of the NIROS device to perform peripheral vascular imaging and identify tissue oxygenation changes in a mouse model with and without induced vascular calcification to determine if it impacts peripheral vascular imaging.

Materials & Methods

NIROS was initially validated using a commercial NIRS device that measures tissue oxygenation (via oxygen saturation). The validation studies were conducted in response to a vascular occlusion test (VOT) in control subjects. The validation was followed by pilot studies on mice model to assess the extent of changes in tissue oxygenation in response to vascular occlusion with and without induced calcification. Herein, the instrumentation of the custom NIROS device and the two studies are described.

Instrumentation

NIROS

A portable continuous wave-based, NIROS was developed to perform non-contact-based spatio-temporal imaging. The source end consists of 4 multi-wavelength light emitting diode (LED) packages (SMT690D/81-/830, Marubeni) containing three semiconductor dies with peak wavelengths at 690, 810, and 830 nm (as reported by the manufacturer). A custom Arduino-based LED driver is used to power the appropriate semi-conductor die for the desired wavelength and number of LEDs. For the current studies, only 690 and 830 nm wavelength were used during imaging and obtaining the hemoglobin-based parameters from the diffuse reflectance signals. The total optical power across the multiple LEDs and at each wavelength is 32mW (point blank). The LEDs are multiplexed between 690 and 830 nm at 2 Hz temporal frequency (equivalent to 1 Hz per wavelength) via a custom LED driver. The optical power of the LEDs reaching the imaged surface is < 5mW across an imaging region. The diffuse reflected NIR signals are obtained at both the wavelengths from the tissue surface. These signals are optically filtered through a 645 nm long pass filter (LP 645-M27, Midwest Optical Systems Inc.) that blocks light below 620 nm ($< 5\%$ transmission) and passes light ≥ 660 nm with $90 + \%$ transmission. The focusing lens (HF9HA-1B, Fujinon) further focuses the diffusely reflected signals onto a NIR sensitive complementary metal-oxide semiconductor (CMOS) sensor (IDS-UI-3240CP, IDS Imaging Development Systems). A time of flight (ToF) module (VL53L0X, Adafruit) is included in the NIROS system to maintain consistent imaging distance across weeks of treatment. Prior to imaging, the ToF module is used to determine the imaging distance and maintain the distance across repetitions

or comparison studies. During the validation study, all images were acquired at a 15 cm distance, resulting in a 120cm^2 overlap region encompassing the entire target area. A MATLAB-based graphical user interface (GUI) is used to automate the acquisition of the (dual-wavelength) spatio-temporal diffuse reflected maps from the NIROS device. A schematic of our NIROS imaging system is given in Fig. 1A.
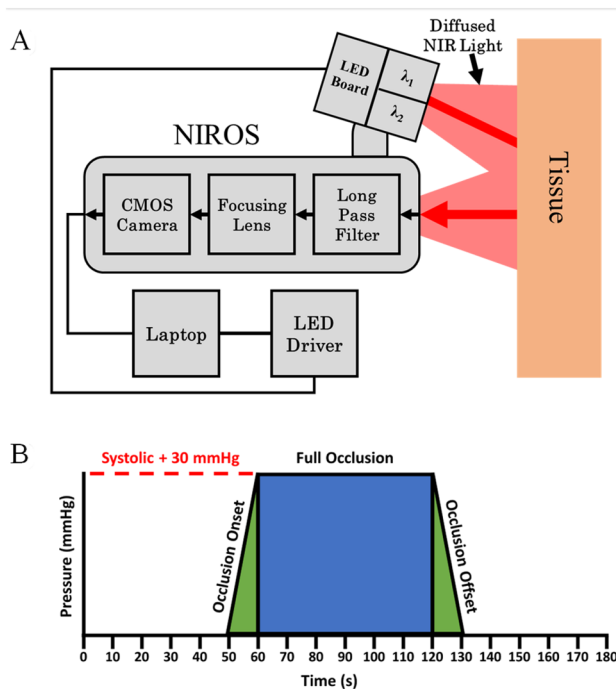
Commercial Device

Validation studies of NIROS were performed in comparison to Snapshot$_{NIR}$ (Kent Imaging), which provides spatial maps of oxygen saturation (or tissue oxygenation) via non-contact NIRS imaging. Unlike our NIROS device that performs dynamic imaging (at 1 Hz per wavelength), the commercial device is limited to static imaging as snapshots of oxygen saturation maps that can be acquired every 10 s (0.1 Hz frequency) manually. For validation purposes, the spatio-temporal maps of tissue oxygenation from NIROS (every 10 s) were compared to that obtained from the commercial device. The commercial device was not used for pilot mice imaging studies. This is because the commercial NIRS device is only capable of spatial mapping of tissue

Fig. 1 A Schematic of NIROS device. The time-of-flight (ToF) module to measure imaging depth is an add-on and can be detached from NIROS as needed. **B** Vascular occlusion protocol used for control subjects. At $t = 50$ s pressure is applied via the sphygmomanometer until pressure is equal to the subject's measured systolic pressure $+ 30$ mmHg. At $t = 60$ s maximum pressure is reached and maintained until $t = 120$ s and released immediate after. The control subjects were imaged for a total of 180 s

oxygenation but has a poor temporal resolution (0.1 Hz) to map for dynamic microcirculatory flow changes (every second) during mice imaging.

In Vivo Validation Study via VOT

The gold-standard VOT was carried out in vivo on control subjects and imaged using NIROS and a commercial NIRS device. The measured oxygen saturation changes from both devices were then correlated. In general, vascular occlusion, as a stimulus, is well defined and contains characteristic signal features with regards to hemoglobin-based oxygenation measurements. Due to the repeatability of the VOT-based stimulus in vivo, it has been typically applied to assess either the oxygen reserve or perfusion in conditions such as: shock, hypovolemia, and septic shock [7, 10, 26]. VOTs utilize a pneumatic cuff fixated onto the subject's upper arm to halt blood circulation for a duration of time before quickly deflating the cuff after the duration threshold has been met. When inflated to pressures 30 mmHg above an individual's systolic blood pressure, the cuff creates an occlusion where arterial and venous circulation is ceased, and oxygen desaturation occurs due to tissue cells utilizing the remaining oxygen in the arm [9].

Subject Recruitment and Imaging Protocol

Three control subjects between the ages of 19–31 were recruited and imaged with IRB approval from the university IRB (#13-0092). The recruited subjects consisted of two females and one male, with a Fitzpatrick skin type of I. Fitzpatrick skin type was confirmed by referencing the imaged tissue against a standard Fitzpatrick skin color scale [13]. All subjects were imaged on the dorsum of their left hand using the same occlusion protocol, as illustrated in Fig. 1B. The occlusion protocol was 180 s long and consisted of 50-s of initial rest, 10-s of occluding, 60-s of occlusion, and 60-s of recovery after occlusion.

Image Acquisition

Prior to imaging, each subject's blood pressure was measured thrice (using a digital sphygmomanometer), and the highest value was recorded as the subject's systolic pressure. A pressure 30 mmHg greater than the subject's systolic blood pressure was used to induce total vascular occlusion (using a manual sphygmomanometer). Imaging was performed on the dorsum of the left hand in a dark room setting, with subjects seated upright and the palm of the hand placed flat on the table. The nail bed of each digit was covered with black masking tape to prevent reflection. Fiducial markers were placed on the fingers of each subject for spatial referencing. Custom mounts were used to position both devices

(NIROS and the commercial device) parallel to and ~15 cm from the hand. A diffusely reflective calibration sheet (white cardstock) was imaged to capture reference images with each device prior to in vivo data acquisition. NIROS and the commercial device acquired the data sequentially across the 180 s of the occlusion protocol at 1 Hz and 0.1 Hz temporal resolution, respectively, with a 15-min interval between recordings.

Image Analysis

The various steps in the image analysis are as described below.

(I) *Image co-registration* During the imaging studies, both the NIROS and the commercial device were fixated to a custom mount to maintain the same imaging distance across subjects and repetitions and to keep the devices' steady. In addition, once each subject had their hand comfortably situated onto the imaging table, subjects were required not to move their hand once the first recording started.

Image co-registration was conducted as an additional tool to eliminate any potential movement. As described, NIROS was used to acquire 690 nm and 830 nm image sets of the tissue data. The first NIR image from each set was designated as the fixed, non-moving, image. An automated, intensity-based, co-registration approach was applied to align each subsequent image to the fixed image as described by Muthukumaran et al. [29] Transformations were limited strictly to rotational and translational movements.

When calculating oxygenation maps (as described in step (II) below) using the diffuse reflectance maps obtained from NIROS, the appropriate image transformations were applied to the calibration image set for each timepoint to ensure the correct reference signal was used at each pixel location. In the commercial device, the same co-registration approach was applied to the oxygen saturation maps (since that is the only output obtained from the device).

(II) *Calculation of spatial–temporal oxygenation maps* The Modified Beer-Lambert's Law (MBLL) was used to calculate spatio-temporal maps of effective tissue oxygenation via hemoglobin-based parameters (oxy- ΔHbO, deoxy- ΔHbR, total hemoglobin HbT, and oxygen saturation StO$_2$) from the diffuse reflectance signals obtained at both the wavelengths [1, 22, 23, 38]. The change in optical density $\Delta OD_{t=n}(x, y, \lambda_i)$ at each wavelength was calculated for each spatial coordinate (x,*y*) at each wavelength

λ_i and for each time point (*t*) from the diffuse reflectance signals at each wavelength ($I^{\lambda i}(,x,y,t)$ after accounting for the dark noise ($I_D(x,y)$) and calibration factor ($I_{cal}{}^{\lambda i}(,x,y,t)$).

$$\Delta OD_{(x,y,t)}^{\lambda i} = -log\frac{I_{(x,y,t)}^{\lambda i} - I_D(x,y)}{I_{cal(x,y,t)}^{\lambda i} - I_D(x,y)} \quad (1)$$

Using this optical density at both wavelengths, extinction coefficient for oxy-hemoglobin, $\epsilon_{HbO}(\lambda_i)$, and deoxy-hemoglobin, $\epsilon_{HbR}(\lambda_i)$, the path length factor, B at the imaged wavelength (λ_i), and the inter-optode distance, L between the source and detector, the spatio-temporal maps of HbO and HbR were in turn calculated from respectively:

$$[HbO](x,y,t) = \frac{\epsilon_{HbR}^{\lambda 1}\frac{\Delta OD_{(x,y,t)}^{\lambda 2}}{B_{(x,y)}^{\lambda 2}} - \epsilon_{HbR}^{\lambda 2}\frac{\Delta OD_{(x,y,t)}^{\lambda 1}}{B_{(x,y)}^{\lambda 1}}}{\left(\epsilon_{HbR}^{\lambda 1}\epsilon_{HbO}^{\lambda 2} - \epsilon_{HbR}^{\lambda 2}\epsilon_{HbO}^{\lambda 1}\right)L} \quad (2)$$

$$[HbR](x,y,t) = \frac{\epsilon_{HbO}^{\lambda 2}\frac{\Delta OD_{(x,y,t)}^{\lambda 1}}{B_{(x,y)}^{\lambda 1}} - \epsilon_{HbO}^{\lambda 1}\frac{\Delta OD_{(x,y,t)}^{\lambda 2}}{B_{(x,y)}^{\lambda 2}}}{\left(\epsilon_{HbR}^{\lambda 1}\epsilon_{HbO}^{\lambda 2} - \epsilon_{HbR}^{\lambda 2}\epsilon_{HbO}^{\lambda 1}\right)L} \quad (3)$$

In the current studies, B and L are assumed to not changing with wavelength or time, and hence are grouped to obtain the effective or relative changes in HbO and HbR as $\Delta[HbO](x,y,t) = [HbO](x,y,t)$ *LB* and $\Delta[HbR](x,y,t) = [HbR](x,y,t)LB$. The total hemoglobin (ΔHbT) and oxygen saturation (ΔStO$_2$) were in turn calculated as given by Eqs. 4 and 5.

$$\Delta[\text{HbT}](x,y,t) = \Delta[HbO](x,y,t) + \Delta[HbR](x,y,t) \quad (5)$$

$$\Delta[StO_2](x,y,t) = \Delta[HbO](x,y,t)/\Delta[\text{HbT}](x,y,t) \quad (6)$$

Similar hemoglobin-based parameters were acquired from diffuse reflectance images during cortical imaging studies in animal models [11, 21, 39].

(III) *Time syncing data* The temporal frequency from the commercial device was restricted to 0.1 Hz, or one image acquired every 10 s. Oxygenation maps from NIROS were extracted at equivalent timepoints and used for further processing.

(IV) *Spatial rescaling* While imaged at similar distances, the image scale from NIROS and the commercial device differed. The image scale was calculated from each device across all sets using the square fiducial marks of known 6×6 mm dimensions.

Images were rescaled with respect to the oxygenation map set with the lowest scale across each subject.

(V) *Occlusion-induced hemoglobin concentration profiles* A 4×4 cm region of interest was chosen from the dorsum of the hand for each subject (Fig. 2A). The region of interest was further divided into four 2×2 cm quadrants (Fig. 2B). In each quadrant, twenty-five, non-repeating, 5×5-pixel subregions were randomly selected (Fig. 2C) and averaged individually across time to produce 25 trendlines. The Savitzky-Golay filter was applied to smoothen each signal while preserving the trend (Fig. 2D). The average oxygenation signal, in terms of ΔHbO, ΔHbR, ΔHbT, and ΔStO$_2$, was calculated for each quadrant, and then recalculated as the percent change in signal with respect to occlusion onset ($t = 60$ s) (Fig. 2E). The average occlusion-induced oxygenation changes were obtained by averaging across all four quadrants within each subject. The standard error at each imaged timepoint was also calculated, using the average occlusion-induced oxygenation changes across all quadrants within each subject.

(VI) *Pearson's-based correlation coefficient* The Pearson's-based correlation coefficient (PCC) was calculated using the average hemoglobin-based concentration profiles from each quadrant and used to correlate the extent of synchrony in oxygenation flow changes across quadrants and subjects.

The PCC of the measured oxygen saturation were compared pairwise between quadrants within each subject and device (NIROS and commercial). In addition, PCC of the measured oxygen saturation obtained from matching quadrants (inter-quadrant) of each subject was compared between the two devices.

Following the validation studies to demonstrate that NIROS can map the tissue oxygenation changes in response to the standard occlusion test, peripheral vascular imaging studies were performed to assess the feasibility of NIROS to differentiate mice with and without the presence of vascular calcification.

Peripheral Vascular Imaging in Mice: A Feasibility Study

A peripheral vascular feasibility imaging study was performed on mice with vascular calcification induced via a high phosphate diet. In this model, CKD was induced in adult mice by feeding them a high adenine diet (0.2%) for 6 weeks [4, 35]. At week-6, the high-adenine diet was supplemented with high phosphate (1.8%) to also induce vascular calcification. A peripheral vascular occlusion test was carried out before (week-6) and after (week-12) the addition of the high phosphate to the adenine diet, and the mice were imaged using NIROS. Differences in hemoglobin concentration maps in response to peripheral occlusion were compared before and after the onset of vascular calcification.
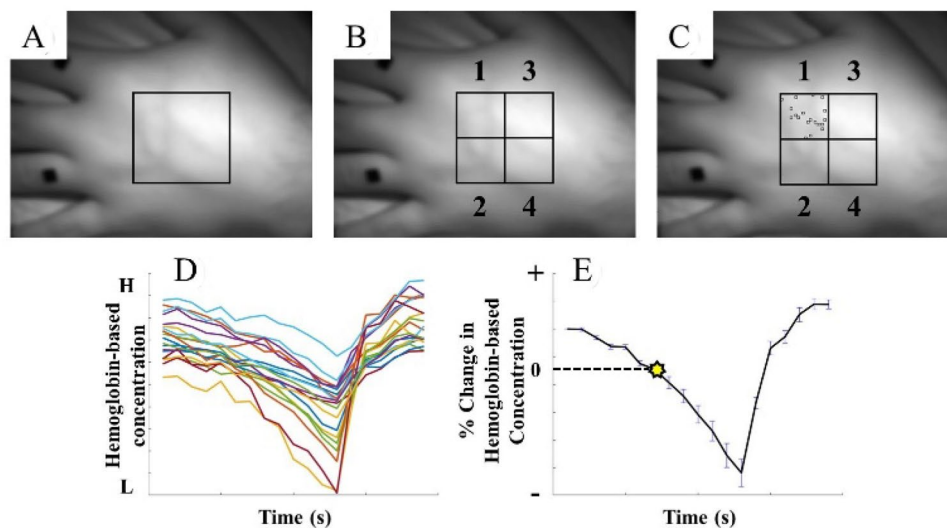
Fig. 2 Methodology to extract the hemoglobin concentration profile in response to VOT from the dorsum of the left hand. The steps include: **A** A region of interest was selected from the dorsum of the hand for each image set. **B** The ROI was broken up into four quadrants. **C** 25 sub-ROIs were selected and **D** used to calculate 25 hemoglobin-based concentration profiles across time. The Savitzky-Golay filter was applied to calculate the average signal at each quadrant. The averaged signals in each quadrant were recalculated as the percent change in signal with respect to occlusion onset (@ $t = 60$ s)—and visually denoted by the yellow filled asterisk in (**E**)

Mouse Model of CKD-Induced Vascular Calcification

At 10 weeks of age, ten C57BL/6J mice were placed on a 0.2% adenine diet for six weeks to induce CKD. For the remaining 6 weeks of the study, the diet was supplemented with 1.8% phosphate to induce vascular calcification, a pathological feature common in CKD-induced vascular dysfunction. Mouse weight was monitored and recorded throughout the study and considered in analysis. Three mice died prior to week-12 and two mice had data acquisition errors. Hence, only five mice were assessed in the current study on peripheral vascular imaging in response to vascular calcification.

Data Acquisition and Analysis

NIROS was used to perform peripheral vascular imaging of the mouse tails (dorsal side) in response to an occlusion protocol. The device acquired spatio-temporal maps at week-6 (prior to adding high phosphate and without the presence of vascular calcification) and at week-12 of the diet. The mice were placed in a prone position, temperature controlled, and anesthetized using isoflurane throughout data acquisition. Imaging was carried out at 2Hz frequency by multiplexing between the two source wavelengths (690 and 830 nm) for 10 min. For the first 5 min, mice were imaged while their body temperature stabilized and without applying any occlusion. During the following 5 min, a tail-cuff (at the base of the tail) was used to occlude the tail. A systematic occlusion cycle was generated using a Kent CODA blood pressure monitor device with a consistent maximum occlusion pressure of 250 mmHg. The tail was occluded seven times using a 60-second stimulus cycle (12s from rest to full occlusion, 3s occlusion, 15s for deflation, and 30s-rest) (Fig. 3A). The dynamically changing diffuse reflectance NIR measurements (at both the source wavelengths) were obtained in response

to the occlusion cycles. The occlusion protocol remained the same for both week-6 and week-12 of the study.

A diffusely reflective calibration sheet was used prior to each imaging session to obtain the reference NIR signals (similar to in vivo validation study in Sect. 2.2.3). The effective hemoglobin-based concentration maps (in terms of $[\Delta HbO]$, $[\Delta HbR]$, $[\Delta HbT]$, and $[\Delta StO_2]$) were calculated using MBLL on the time-varying diffusely reflected NIR maps (similar to the in vivo validation study in Sect. 2.2.3). There were no motion artifacts; hence, image coregistration across the time-varying signal was not performed. Changes in the effective hemoglobin parameters with respect to time were determined at a selected region of interest (ROI) (Fig. 3B). The average spatial ΔHbT was used to determine the area of largest concentration as the vessel with blood flow. The ROI (4×4 pixels) was chosen as the spatially centered location with this largest ΔHbT concentration on the tail (red region in Fig. 3b). The 16-pixels within the ROI were averaged to have one trend of the area. Three ROIs were chosen on the tail's blood vessel for each mouse and averaged to determine the variability of the measured oxygen saturation (with each mouse).

Hemoglobin-based parameters were normalized by calculating the percentage of change with reference to the respective parameters 60 seconds prior to the start of the occlusion cycles. The time-synchronized trendlines for the oxygenation parameters were compared for a qualitative assessment of the blood flow without the presence of calcification (week-6). The evaluation of all parameter responses analogized the occlusion on a mouse model with a human. Further analysis included the comparison of the absence of calcification (week-6) and the presence of calcification (week-12). With the week-6 and -12 trendlines, the extent of change was quantified per parameter. The extent of change was calculated by the difference in the percentage change
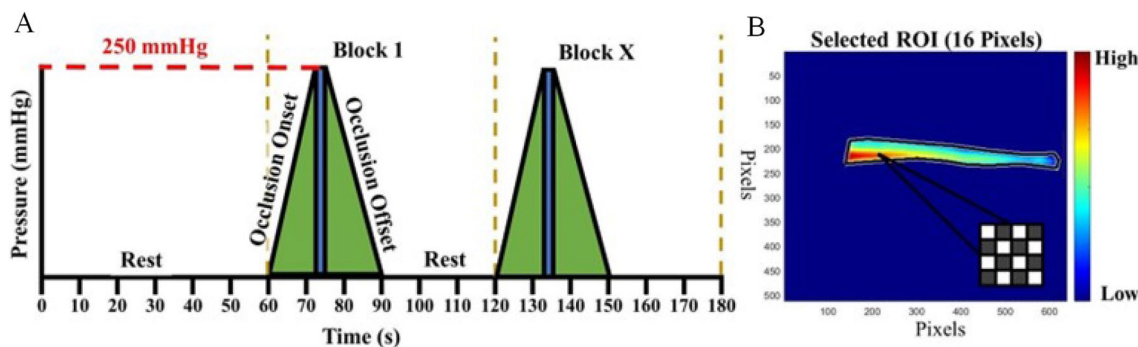
Fig. 3 **A** Vascular occlusion protocol used for imaging the mouse tail. At $t = 60$ s the cuff on the mouse tail applied pressure until reaching peak of 250 mmHg at $t = 72$ s. Occlusion pressure was maintained for 3 s, then steadily released until $t = 90$ s. The occlusion cycle started after a 30 s rest period. A total of 7 occlusion cycles were performed and imaged. **B** Sample average hemoglobin-based concentration map

of the mouse tail. The map was used to identify the blood vessel (the red–orange region) during the dynamic imaging session. The region of interest (ROI) was the selected area (4×4 pixels) within the tail's blood vessel. Three different ROIs were chosen within the mouse's tail vessel and its average and standard deviation was determined

when the occlusion pressure reached its peak (250mmHg) and the plateau value that followed (0 mmHg).

Results

In Vivo Validation of NIROS via VOT Studies on Control Subjects

The overall average of the measured tissue oxygenation profiles in terms of: ΔHbO, ΔHbR, ΔHbT, and ΔStO_2, across all subjects and quadrants, are plotted in Fig. 4. Each measured hemoglobin-based parameter was normalized with respect to their corresponding parameter at the onset of the first occlusion cycle (i.e. at $t = 60$ s).

During occlusion, it was observed that, on average the ΔHbR increase by 10% and ΔStO_2 fell by 4%. ΔHbO and ΔHbT experienced a ~ 2% decrease and increase, respectively. The largest change in ΔHbO, ΔHbR and ΔStO_2 was observed post-occlusion during the recovery phase. ΔHbO and ΔStO_2 increased to beyond baseline (pre-occlusion levels), whereas ΔHbR fell below the baseline. There was an increase in ΔHbT during post-occlusion for a brief period of ~ 10 s before it began to decrease. Overall, the nature and extent of changes of each tissue oxygenation parameter were similar across all subjects.

Correlation of Occlusion-Induced Oxygen Saturation Changes Within Device

The PCCs were calculated in a pair-wise manner using the average oxygen saturation measurements obtained from all four quadrants (Q1 to Q4) within each subject and device used and is given in Table 1. It was observed that, on average, the correlation was greater than 97% for each pairwise comparison for both devices and across all subjects.

The correlation in the temporal oxygenation changes (in terms of oxygen saturation) was compared between the devices within each quadrant and subject (Table 2). It was observed that the temporal changes in oxygen saturation was highly correlated (overall > 95%) across all subjects and quadrants.

Correlation of Occlusion-Induced Oxygen Saturation Changes Between Devices

The occlusion-induced temporal oxygen saturation changes across the two devices using the averaged measurements obtained from all 4 quadrants and 3 subjects is given in Fig. 5. The normalized oxygen saturation obtained from NIROS (orange) and the commercial device (blue) are plotted with the standard error calculated at each timepoint measurement. Each oxygen saturation signal is plotted with
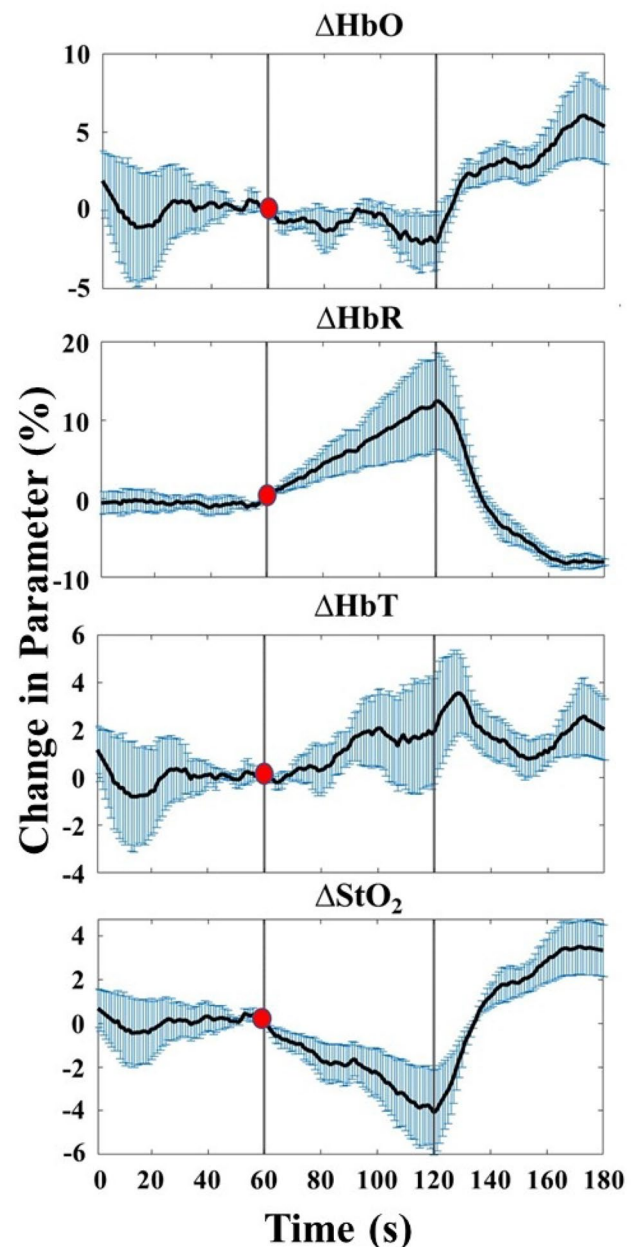
Fig. 4 Average tissue oxygenation changes (in terms of ΔHbO, ΔHbR, ΔHbT, and ΔStO_2) across all subjects and their four quadrants in response to VOT. All parameters were normalized with respect to the respective parameters at the onset of the occlusion cycle (i.e. at $t = 60$ s), as given by the red dot. The blue vertical bars denote the standard error in the hemoglobin-based changes at each timepoint and across all the subjects

respect to their own y-axis to illustrate the overall correlation in the oxygenation change observed from each device. Both devices captured a decrease in oxygen saturation during the occlusion period, followed by a reactive hyperemic overshoot common observed during occlusion offset [10].

Upon correlating the average oxygen saturation changes during the occlusion cycle ($t = 60$ s to 180 s) across all the

Table 1 Pearson's correlation coefficient of the measured oxygen saturation between quadrants, in all subjects and using both the devices

Quadrant	Pearson's correlation coefficient (%) between quadrants in each subject and using each device					
	Subject 1		Subject 2		Subject 3	
	NIROS	Commercial Device	NIROS	Commercial Device	NIROS	Commercial Device
Q1 v Q2	99.1	99.9	98.4	99.0	99.6	94.8
Q1 v Q3	99.4	99.3	98.1	98.1	99.7	96.9
Q1 v Q4	99.7	99.8	99.4	99.6	99.3	98.5
Q2 v Q3	99.4	99.0	94.1	94.8	99.9	97.5
Q2 v Q4	99.6	99.8	96.5	97.9	99.3	97.2
Q3 v Q4	99.3	99.0	99.3	99.1	99.4	96.7
Overall average	99.4 ± 0.2	99.5 ± 0.4	97.6 ± 2.0	98.1 ± 1.7	99.5 ± 0.2	97.0 ± 1.2

Table 2 Pearson's correlation coefficient of the measured oxygen saturation for each subject and quadrant when compared between NIROS and the commercial device

Quadrant	Inter-Quadrant Pearson's correlation coefficient across devices (%)		
	Subject 1	Subject 2	Subject 3
1	97.5	96.2	94.2
2	97.8	94.2	91.9
3	96.1	96.2	91.0
4	97.7	95.5	94.0
Subject average	97.3 ± 0.8	95.5 ± 0.9	92.8 ± 1.6
Overall average	95.2 ± 2.2		

Table 3 Pearson's correlation coefficient of the oxygen saturation signal between the two devices, averaged across all four quadrants in each subject

Subject	1	2	3	Grand average
PCC (%)	97.5	96.0	94.2	95.9 ± 1.7

section. Since pattern was the same, a larger sample size would have only brought the overall error down. However, our study already demonstrated the pattern in response to occlusion being the same across the quadrants and subjects, and hence the study was not continued on a larger sample size.

## Feasibility Study of Peripheral Vascular Imaging in Mice with and without Vascular Calcification

The changes in tissue oxygenation parameters (in terms of ΔHbO, ΔHbR, ΔHbT, and ΔStO_2) across the rest period and the first occlusion cycle from one sample case of the mouse model prior to vascular calcification (i.e., at week-6) is shown in Fig. 6A. A distinct increase in ΔHbO, ΔHbR, and ΔHbT with the onset of occlusion was observed. These three parameters decreased at the pressure release point; however, ΔHbR was the only one to return to baseline. ΔStO_2 slightly increased, but in comparison to the other parameters, it was least impacted from occlusion, possibly because the mouse tail did not reach ischemic state with the short occlusion cycle.

Extracted tissue oxygenation parameters were compared between week-6 (prior to vascular calcification) and week-12 (with the onset of vascular calcification) groups, as shown in Fig. 6B. The changes in ΔHbO, ΔHbR, and ΔHbT were distinct in response to occlusion at week-6. However, this response was vaguely seen in the mice upon onset of calcification (at week-12). The occlusion protocol was maintained the same for both week-6 and week-12. Hence, the lack of
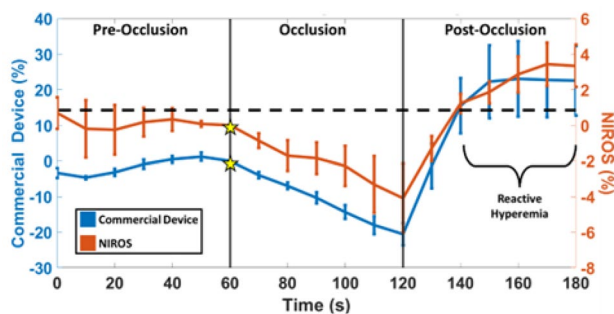
Fig. 5 ΔStO_2 profile (%) in response to occlusion using NIROS and the commercial device, averaged across all quadrants and subjects. The standard error in measurement at each timepoint is plotted for the respective device. The data was initialized and normalized with respect to the timepoint at the onset of occlusion (@ $t = 60$ s), shown by the yellow star

four quadrants in each subject (as given in Table 3), it was observed that the overall correlation between the two devices was > 95%. These validation studies were followed by feasibility peripheral vascular imaging studies on mice with and without vascular calcification as described in the next
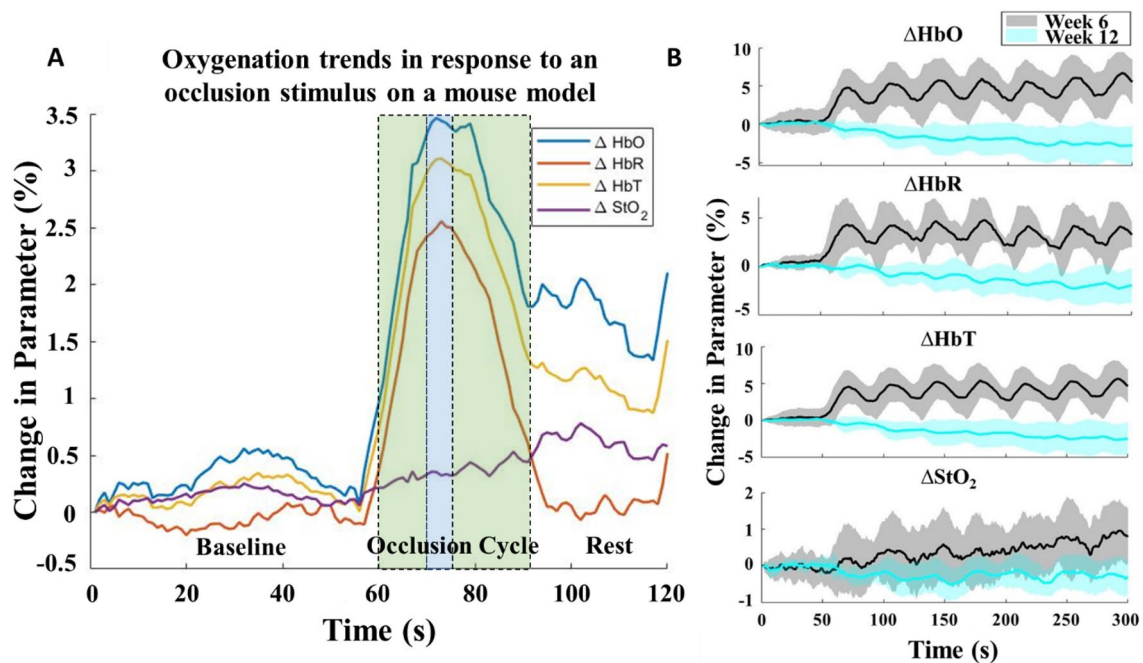
Fig. 6 **A** Sample tissue oxygenation trendlines in response to an occlusion stimulus on a mouse model. The trendlines were extracted from the selected ROI (as shown in Fig. 4), of a sample mouse prior to the onset of calcification (i.e. week-6). Rest period for the mouse took place for the first 60 s (baseline) and the occlusion stimulus with a tail cuff began at 60 s. Initial green shading represents the increase in pressure (10 s), followed by blue shading where max pressure of 250 mmHg is maintained (5 s). Second green shading is the release of pressure until 0 mmHg (15 s) is exerted, continued by rest (30 s). **B** Average tissue oxygenation trendlines in terms of ΔHbO, ΔHbR, ΔHbT, and ΔStO_2 across all five mice during week-6 (prior to calcification) and week-12 (onset of calcification). Rest period for the mouse took place for the first 60 s and the occlusion cycles on the tail began immediately after. The shaded region relates to the standard error across different mice at both timepoints (week-6 and week-12)

response to the occlusion in week-12 is possibly due to the presence of vascular calcification. The variability (or standard error) among the cohort as observed distinctly in week-6 is possibly due to differences in body weight and biological sex of these mice. Despite the variance amongst mice, we observed similar waveform changes across the mice during both week-6 and week-12. This small feasibility study on 5 mice clearly distinguished the two mice groups (at week-6 prior to and week-12 with onset of calcification).

Discussion

In Vivo Validation Studies

VOT occlusion duration is defined either as a specified period of time or until an oxygen desaturation value has been met [9]; with fixed time durations often chosen as there are fewer complications when comparing responses. Occlusion durations of 3- or 5- min are common, however, there is no standardized way to perform a VOT [9, 27]. Occlusion and oxygen desaturation occur immediately once full pressure has been applied and cells begin to consume the remaining oxygen reserves. Our current validation studies observed that the ΔHbO and ΔStO_2 decreased during occlusion and rebound upon occlusion offset as report in literature [12]. Inversely, ΔHbR concentrations increased during occlusion and decreased upon occlusion offset.

The ΔHbT, on average, increased before beginning to stabilize ~ 40 s in the occlusion phase (around the 100th second of the plots presented in Fig. 4). The increase in ΔHbT measured from the limb may also reflect blood pooling due to total venous occlusion. As most VOT studies tend to use longer occlusion periods, the one minute of occlusion used here may have primarily captured the blood volume in the limb reaching a steady state. Upon occlusion offset, ΔHbO and ΔStO_2 increased, whereas ΔHbR decreased, beyond baseline levels as part of the hyperemic reperfusion response. Interestingly, ΔHbT only experiences a slight increase after occlusion offset for about 10 s. The brief hyperemic reperfusion in ΔHbT may reflect the initial influx of renewed blood before vascular tone changes to return to a more typical level of perfusion.

While the above observations were made based on the overall changes in tissue oxygenation parameters across all subjects and imaged quadrants, the dorsal of the hand has

an inhomogeneous distribution of superficial vascular structures that varies in spatial density by subject. An example of this is visually observable from the NIR image in Fig. 2C between Quadrants 1 & 2 vs 3 & 4. Through pairwise correlational analysis of ΔStO_2 changes between quadrants, it was observed that all quadrants in each subject shared > 94% correlation. This indicates that regardless of vascular density, all points of the hand experience a similar response to occlusion-induced changes. Further, when comparing within the same quadrant between NIROS and the commercial device, the overall correlation across all quadrants was greater than 95%. Both devices could image and measure the decrease in ΔStO_2 during the occlusion cycle and the hyperemic reperfusion that commonly proceeds post-occlusion [12, 33].

It was observed that while the overall ΔStO_2 trend was visually similar between devices (Fig. 5), the measured values differed (probably from different models used). NIROS imaged the dorsum of the hand under two NIR wavelengths (690 nm and 830 nm) and utilized mBLL to calculate hemoglobin-based tissue oxygenation parameters. The commercial device, on the other hand, utilized four NIR wavelengths (670, 730, 890, and 940 nm). While the exact data analysis approach is not known from the commercial device (proprietary), NIR images from all four wavelengths were possibly used to calculate the oxygen saturation maps. However, regardless of tissue region and size, NIROS captured an occlusion-induced oxygen saturation response with > 95% correlation to the commercial device. Thus, NIROS was validated to obtain similar time-varying trends in oxygen saturation with the added advantage of performing spatial–temporal imaging at a faster rate (10x) than the commercial device. This fast rate of data acquisition is highly essential when using a NIRS device for capturing the dynamically varying tissue oxygenation changes in response to occlusion. This is possible using our dynamically imaging NIRS device (such as NIROS) compared to a static imaging NIRS device (such as the commercial device). Future work involves further improving the temporal resolution of NIROS from 1 Hz to 5–10 Hz to also capture tissue oxygenation changes at the rate of the heart beat (> 300 beats per minute in mice and ~ 72 beats per minute in humans).

Peripheral Vascular Imaging Studies

Cardiovascular disease is the leading cause of death in individuals with chronic kidney disease (CKD), and vascular calcification is the best predictor of CKD-associated cardiovascular morbidity [18, 24]. Individuals with CKD also exhibit peripheral vascular dysfunction, and vascular calcification can occur in peripheral arteries [5, 8, 30]. Even without mineral deposition, calcification in larger arterial beds may alter blood flow patterns and perfusion throughout systemic circulation. Low-cost techniques that assess

peripheral vascular dysfunction could potentially replace expensive imaging techniques (such as computed tomography or magnetic resonance angiography) for regular monitoring of cardiovascular health in CKD patients.

The development of a low-cost, non-invasive technique to assess the onset of vascular calcification via peripheral vascular imaging in human subjects could potentially enhance risk stratification and enable the advent of therapies to improve cardiovascular health. To date, no study has focused on assessing the microcirculatory changes in peripheral vascular tissue oxygenation in mice before and after the onset of vascular calcification.

In this NIRS imaging study, prior to calcification (week-6), occlusion resulted in an initial increase in oxygenation parameters (ΔHbO, ΔHbR, and ΔHbT) as shown in Fig. 6. The tail occlusion in these mouse models is expected to cause a total occlusion (both arteries and veins) as the maximum occlusion pressure was 250 mm Hg (well above arterial pressures). The changes in tissue oxygenation parameters typically follow the trend shown in Fig. 7, as observed in prior studies on the hind limbs of rabbits [17]. In our studies, we observed that all the tissue oxygenation parameters increased upon occlusion, unlike a decrease in oxy-hemoglobin as observed in the hind limbs of rabbits. This difference in the hemodynamic response could be from the 2-min occlusion performed in the past studies on rabbits compared to a maximum of 5 s occlusion in our mouse models. Interestingly, the total hemoglobin was shown to
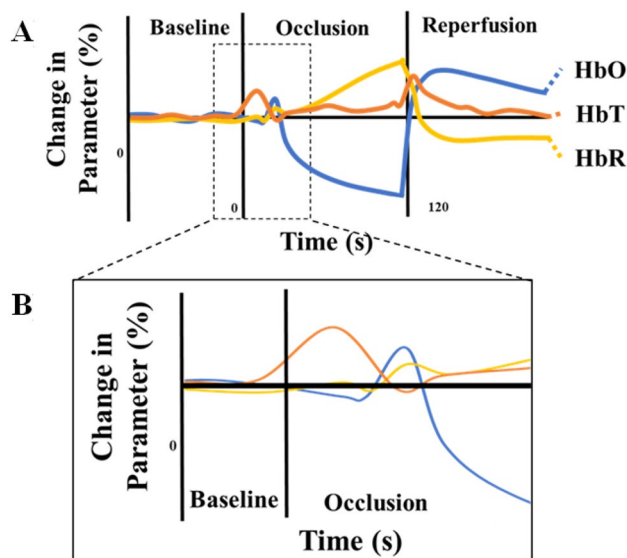
Fig. 7 **A** Typical total vascular occlusion-induced oxygenation change in terms of oxy- (HbO), deoxy- (HbR), and total hemoglobin (HbT) as observed from prior studies on the hind limbs of rabbits. Adapted from Irwin (1995). **B** The zoomed in trendlines within the first few seconds of occlusion onset, to demonstrate the immediate increase in HbT

increase immediately upon the onset of occlusion (as shown in Fig. 7B), which is similar to what we observed within the 5-s occlusion as well. The mice are smaller animals, and attempting to occlude them for longer periods of times, as in rabbits, may result in their death. Finding the optimal time to occlude a mouse tail that would allow us to observe similar changes in oxygenation parameters seen in humans without distressing or causing injury to the mice needs to be explored.

The changes in ΔHbO, ΔHbR and ΔHbT were observed in response to occlusions in mice at both the time points (prior to and with onset of vascular calcification at week-6 and -12, respectively). However, the extent of change significantly diminished from week-6 to week-12 with the onset of vascular calcification. The extent of change in ΔHbT in response to occlusion (area under the curve) possibly relates to the total blood volume, similar to the direct relation of ΔHbT to the cerebral blood volume in brain imaging studies using NIRS [6, 16, 31, 36]. The drop in the ΔHbT response from week-6 to week-12 (with the onset of vascular calcification) can also imply a change in the total blood volume in the peripheries.

The ΔStO_2 in this study did not change significantly in response to the multiple occlusion cycles, indicating that the occlusion was not maintained for sufficient time to bring the tail to an ischemic state. The time the mice remained in the total occlusion state was ~5 s, which was possibly not sufficient for the tail to reach the complete ischemic state or even cause a significant change in oxygen saturation during each occlusion cycle. However, there was a slight overall increase in ΔStO_2 across the occlusion cycles as seen from Fig. 6. The reason for this gradual yet slight increase in ΔStO_2 will be explored with further extensive studies.

Interestingly, there was no distinct drop in the blood pressure of these mice from week-6 to week-12. At week-6, the mice had the following blood pressure averages ($\pm$ SEM or standard error of measurement): mean arterial pressure of 78.00 ± 2.97 mmHg, diastolic pressure 72.07 ± 2.77, and systolic pressure of 91.13 ± 3.58 mmHg. At week-12, the mice had the following blood pressure averages ($\pm$ SEM): mean arterial pressure of 71.59 ± 2.03 mmHg, diastolic pressure 67.98 ± 1.93, and systolic pressure of 79.45 ± 2.21 mmHg. This possibly implies that the blood pressures are not abnormally low during week-12 and are possibly not the cause for the decreased ΔHbT changes in week-12 from week-6. Similarly, there was no change in the average weight of the mice with a change in diet from week-6 to week-12. The average weight for both weeks was 18.87 g, with week-6 having a range of 17.85–20.55 g and week-12 a range of 15.81–20.69 g. This implies that the decreased ΔHbT changes in week-12 with respect to week-6 is not from weight loss or gain with diet. Additionally, the heart rate

of the mice used in this imaging study was not recorded. Although the heart rate could influence tissue oxygenation, the mouse heart rate is very high (> 300 bpm or > 5 Hz). In our study, the imaging was performed at 1 Hz frequency. Hence, the tissue oxygenation changes in response to the heart rate cannot be captured nor impact our current results due to the high frequency of the heart rate compared to our imaging frequency.

This is a proof-of-concept study to show that we can detect vascular remodeling-associated changes in hemodynamics. For this purpose, we use a mouse model of vascular calcification to identify whether the NIROS device can detect changes in oxygenation of peripheral vessels. The presence of vascular calcification in peripheral arteries increases mortality and limb-specific outcomes [14]. Therefore, it is important to identify and monitor the presence of peripheral vascular calcification. Patients with CKD also exhibit microvascular dysfunction [37], and changes in microcirculation associate with vascular calcification in these patients [32]. Therefore, NIROS-based assessment of superficial hemodynamics may provide a non-invasive approach to gauge general vascular health in CKD patients. On a long term, studies with human subjects will be required to assess the utility of this approach and the relation between microvascular dysfunction and peripheral vascular calcification in patients.

Systemic circulation can be easily monitored using blood pressure cuffs. Although systemic blood pressure can change due to the presence of calcification, there are multiple conditions that can cause systemic changes in blood pressure (heredity, smoking, obesity, etc.). Our data indicates that the NIROS device can be used to detect local changes in tissue oxygenation of peripheral vessels due to the presence of vascular calcification.

Ongoing studies are carried out to correlate peripheral microcirculatory changes in tissue oxygenation and the pathophysiology behind the significant differences observed with onset of vascular calcification in mice. In addition, the optimal occlusion time and pressure to induce a significant change in tissue oxygenation with minimal distress to the mouse will be determined.

In conclusion, a spatio-temporal NIROS was developed to conduct non-contact area imaging of tissues. The in vivo validation studies determined that the oxygen saturation changes in response to the standard VOT between NIROS and a commercial device was > 95% correlated. A pilot study on mice prior to and with the onset of vascular calcification using the NIROS device showed distinct differences in the microcirculatory hemodynamic response in the peripheries. The correlation of these peripheral microcirculatory oxygenation differences to the actual onset of vascular calcification is yet to be explored in our future studies, to positively impact the field of cardiovascular diagnostics.

Declarations

Conflict of interest No benefits in any form have been or will be received from a commercial party related directly or indirectly to the subject of this manuscript.

References

1. Bigio, I. J., and S. Fantini. Quantitative Biomedical Optics: Theory, methods, and applications. Cambridge: Cambridge University Press, 2016. https://doi.org/10.1017/CBO9781139029797.

2. Boezeman, R. P., D. Boersma, J. Wille, J. C. Kelder, M. I. Visscher, F. G. Waanders, F. L. Moll, and J.-P.P. de Vries. The significance of regional hemoglobin oxygen saturation values and limb-to-arm ratios of near-infrared spectroscopy to detect critical limb ischemia. *Vascular*. 24:492–500, 2016.

3. Chiang, N., J. K. Jain, J. Sleigh, and T. Vasudevan. Evaluation of hyperspectral imaging technology in patients with peripheral vascular disease. *J. Vasc. Surg.* 66:1192–1201, 2017.

4. Dargam, V., H. H. Ng, S. Nasim, D. Chaparro, C. I. Irion, S. R. Seshadri, A. Barreto, Z. C. Danziger, L. A. Shehadeh, and J. D. Hutcheson. S2 Heart Sound Detects Aortic Valve Calcification Independent of Hemodynamic Changes in Mice. *Front. Cardiovasc. Med.* 9:809301, 2022.

5. Fowkes, F. G. R., D. Rudan, I. Rudan, V. Aboyans, J. O. Denenberg, M. M. McDermott, P. E. Norman, U. K. Sampson, L. J. Williams, G. A. Mensah, and M. H. Criqui. Comparison of global estimates of prevalence and risk factors for peripheral artery disease in 2000 and 2010: a systematic review and analysis. *Lancet*. 382:1329–1340, 2013.

6. Franceschini, M. A., S. Thaker, G. Themelis, K. K. Krishnamoorthy, H. Bortfeld, S. G. Diamond, D. A. Boas, K. Arvin, and P. E. Grant. Assessment of infant brain development with frequency-domain near-infrared spectroscopy. *Pediatr Res.* 61(5 Pt 1):546–551, 2007.

7. Futier, E., S. Christophe, E. Robin, A. Petit, B. Pereira, J. Desbordes, J.-E. Bazin, and B. Vallet. Use of near-infrared spectroscopy during a vascular occlusion test to assess the microcirculatory response during fluid challenge. *Crit. Care*. 15:R214, 2011.

8. Garimella, P. S., and A. T. Hirsch. Peripheral artery disease and chronic kidney disease: clinical synergy to improve outcomes. *Adv. Chronic Kidney Dis.* 21:460–471, 2014.

9. Gerovasili, V., S. Dimopoulos, G. Tzanis, M. Anastasiou-Nana, and S. Nanas. Utilizing the vascular occlusion technique with NIRS technology. *Int. J. Ind. Ergon.* 40:218–222, 2010.

10. Gómez, H., A. Torres, P. Polanco, H. K. Kim, S. Zenker, J. C. Puyana, and M. R. Pinsky. Use of non-invasive NIRS during a vascular occlusion test to assess dynamic tissue O2 saturation response. *Intensive Care Med.* 34:1600–1607, 2008.

11. Grinvald, A., et al. In-vivo optical imaging of cortical architecture and dynamics. In: Modern techniques in neuroscience research, edited by U. Windhorst, H. Johansson, et al., . Berlin: Springer, 1999, pp. 893–969.

12. Hartwig, V., M. Marinelli, F. Rocco, and A. L'Abbate. Assessment of Microvascular Function Using Near-Infrared Spectroscopic 2D Imaging of Whole Hand Combined with Vascular Occlusion Test. *J. Med. Biol. Eng.* 36:87–95, 2016.

13. Ho, B. K., and J. K. Robinson. Color bar tool for skin type self-identification: a cross-sectional study. *J. Am. Acad. Dermatol.* 73:312–313, 2015.

14. Huang, C.-L., I. H. Wu, Y.-W. Wu, J.-J. Hwang, S.-S. Wang, W.-J. Chen, et al. Association of lower extremity arterial calcification with amputation and mortality in patients with symptomatic peripheral artery disease. *PLoS ONE*. 9(2):e90201, 2014.

15. Humeau, A., F. Chapeau-Blondeau, D. Rousseau, M. Tartas, B. Fromy, and P. Abraham. Multifractality in the peripheral cardiovascular system from pointwise hölder exponents of laser doppler flowmetry signals. *Biophys. J.* 93:L59–L61, 2007.

16. Ijichi, S., T. Kusaka, K. Isobe, et al. Developmental changes of optical properties in neonates determined by near-infrared time-resolved spectroscopy. *Pediatr. Res.* 58:568–573, 2005.

17. Irwin, M. S., M. S. Thorniley, C. J. Dore, and C. J. Green. Near infra-red spectroscopy: a non-invasive monitor of perfusion and oxygenation within the microcirculation of limbs and flaps. *Br. J. Plast. Surg.* 48:14–22, 1995.

18. Jankowski, J., J. Floege, D. Fliser, M. Böhm, and N. Marx. Cardiovascular disease in chronic kidney disease: pathophysiological insights and therapeutic options. *Circulation*. 143:1157–1172, 2021.

19. Kagaya, Y., N. Ohura, H. Suga, H. Eto, A. Takushima, and K. Harii. 'Real angiosome' assessment from peripheral tissue perfusion using tissue oxygen saturation foot-mapping in patients with critical limb ischemia. *Eur. J. Vasc. Endovasc. Surg.* 47:433–441, 2014.

20. Khalil, M. A., H. K. Kim, J. W. Hoi, I. Kim, R. Dayal, G. Shrikhande, and A. H. Hielscher. Detection of peripheral arterial disease within the foot using vascular optical tomographic imaging: a clinical pilot study. *Eur. J. Vasc. Endovasc. Surg.* 49:83–89, 2015.

21. Kohl, M., et al. Physical model for the spectroscopic analysis of cortical intrinsic optical signals. *Phys. Med. Biol.* 45(12):3749, 2000.

22. Kwasinski, R., C. Fernandez, K. Leiva, R. Schutzman, E. Robledo, P. Kallis, L. J. Borda, R. Kirsner, F. Perez-Clavijo, and A. Godavarty. Tissue oxygenation changes to assess healing in venous leg ulcers using near-infrared optical imaging. *Adv. Wound Care*. 8:565–579, 2019.

23. Leiva, K., J. Mahadevan, K. Kaile, R. Schutzman, E. Robledo, S. Narayanan, V. Muthukrishnan, V. Mohan, W. Wu, and A. Godavarty. Breath-hold paradigm to assess variations in oxygen flow in diabetic foot ulcers using a non-contact near-infrared optical scanner. *Adv. Wound Care*. 8:386–402, 2019.

24. London, G. M. Arterial media calcification in end-stage renal disease: impact on all-cause and cardiovascular mortality. *Nephrol. Dial. Transplant.* 18:1731–1740, 2003.

25. Ma, K. F., S. F. Kleiss, R. C. L. Schuurmann, R. P. H. Bokkers, Ç. Ünlü, and J.-P.P.M. De Vries. A systematic review of diagnostic techniques to determine tissue perfusion in patients with peripheral arterial disease. *Expert Rev. Med. Devices*. 16:697–710, 2019.

26. Marín-Corral, J., L. Claverias, M. Bodí, S. Pascual, A. Dubin, J. Gea, and A. Rodriguez. Prognostic value of brachioradialis muscle oxygen saturation index and vascular occlusion test in septic shock patients. *Med. Intensiv. (English Edition)*. 40:208–215, 2016.

27. Mayeur, C., S. Campard, C. Richard, and J.-L. Teboul. Comparison of four different vascular occlusion tests for assessing reactive hyperemia using near-infrared spectroscopy. *Crit. Care Med.* 39:695–701, 2011.

28. Mesquita, R. C., M. Putt, M. Chandra, G. Yu, X. Xing, S. W. Han, G. Lech, Y. Shang, T. Durduran, C. Zhou, A. G. Yodh, and E. R.

Mohler. Diffuse optical characterization of an exercising patient group with peripheral artery disease. *J. Biomed. Opt.* 18:057007, 2013.

29. Muthukumaran, D., and M. Sivakumar. Medical image registration: a Matlab based approach. *Int. J. Sci. Res. Comput. Sci. Eng. Inf. Technol.* 2(1):29–34, 2017.

30. Narula, N., A. J. Dannenberg, J. W. Olin, D. L. Bhatt, K. W. Johnson, G. Nadkarni, J. Min, S. Torii, P. Poojary, S. S. Anand, J. J. Bax, S. Yusuf, R. Virmani, and J. Narula. Pathology of peripheral artery disease in patients with critical limb ischemia. *J. Am. Coll. Cardiol.* 72:2152–2163, 2018.

31. Pham, T., K. Tgavalekos, A. Sassaroli, G. Blaney, and S. Fantini. Quantitative measurements of cerebral blood flow with near-infrared spectroscopy. *Biomed. Opt. Express*. 10(4):2117–2134, 2019.

32. Sigrist, M. K., and C. W. McIntyre. Vascular calcification is associated with impaired microcirculatory function in chronic haemodialysis patients. *Nephron Clin. Pract.* 108(2):c121–c126, 2008.

33. Steenhaut, K., K. Lapage, T. Bové, S. De Hert, and A. Moerman. Evaluation of different near-infrared spectroscopy technologies for assessment of tissue oxygen saturation during a vascular occlusion test. *J. Clin. Monit. Comput.* 31:1151–1158, 2017.

34. Suo, S., L. Zhang, H. Tang, Q. Ni, S. Li, H. Mao, X. Liu, S. He, J. Qu, Q. Lu, and J. Xu. Evaluation of skeletal muscle microvascular perfusion of lower extremities by cardiovascular magnetic resonance arterial spin labeling, blood oxygenation level-dependent, and intravoxel incoherent motion techniques. *J. Cardiovasc. Magn. Reson.* 20:18, 2018.

35. Tani, T., H. Orimo, A. Shimizu, and S. Tsuruoka. Development of a novel chronic kidney disease mouse model to evaluate the progression of hyperphosphatemia and associated mineral bone disease. *Sci. Rep.* 7:2233, 2017.

36. Tgavalekos, K., T. Pham, N. Krishnamurthy, A. Sassaroli, and S. Fantini. Frequency-resolved analysis of coherent oscillations of local cerebral blood volume, measured with near-infrared spectroscopy, and systemic arterial pressure in healthy human subjects. *PLoS ONE*. 14(2):e0211710, 2019.

37. Thang, O. H., E. H. Serné, M. P. Grooteman, Y. M. Smulders, P. M. Ter Wee, G. J. Tangelder, and M. J. Nubé. Premature aging of the microcirculation in patients with advanced chronic kidney disease. *Nephron Extra*. 2(1):283–292, 2019.

38. Yudovsky, D., A. Nouvong, and L. Pilon. Hyperspectral imaging in diabetic foot wound care. *J. Diabetes Sci. Technol.* 4:1099–1113, 2010.

39. Zepeda, A., C. Arias, and F. Sengpiel. Optical imaging of intrinsic signals: recent developments in the methodology and its applications. *J. Neurosci. Methods*. 136(1):1–21, 2004.